Modelling hydrologic impacts of light absorbing aerosol deposition on snow at the catchment scale

Felix N. Matt[1], John F. Burkhart[1, 2], and Joni-Pekka Pietikäinen[3]

[1]Department of Geosciences, University of Oslo, Oslo, Norway
[2]Statkraft AS, Norway
[3]Finnish Meteorological Institute, Helsinki, Finland

Correspondence to: Felix N. Matt (f.n.matt@geo.uio.no)

Abstract. Light absorbing impurities in snow and ice (LAISI) originating from atmospheric deposition enhance the snow melt by increasing the absorption of short wave radiation. The consequences are a shortening of the snow duration due to increased snow melt and, on a catchment scale, a temporal shift in the discharge generation during the spring melt season. In this study, we present a newly developed snow algorithm for application in hydrolgical models that allows for an additional class of input

5   variables: the deposition rate of various species of light absorbing aerosols.

To show the sensitivity of different model parameters, we first use the model as 1-D point model forced with representative synthetic data and investigate the impact of parameters and variables specific to the algorithm determining the effect of LAISI. We then demonstrate the significance of the additional forcing by simulating black carbon deposited on snow of a remote south Norwegian catchment over a six years period, from September 2006 to August 2012. Our simulations suggest a significant

10   impact of BC in snow on the hydrological cycle, with an average increase in discharge of 2.5 %, 9.9 %, and 21.4 % for our minimum, central and maximum effect estimate, respectively, over a two months period during the spring melt season compared to simulations where radiative forcing from LAISI is turned off. The increase in discharge is followed by a decrease caused by melt limitation due to faster decrease of the catchment's snow covered fraction in the scenarios where radiative forcing from LAISI is applied. The central effect estimate produces reasonable surface BC concentrations in snow with a strong annual

15   cycle, showing increasing surface BC concentration during spring melt as consequence of melt amplification. However, we further identify large uncertainties in the representation of the surface BC concentration and the subsequent consequences for the snowpack evolution.

1 Introduction

The representation of the seasonal snowpack is of outstanding importance in hydrological models aiming for application in cold

20   or mountainous environments due to various reasons. First of all, in many mountainous and high mountain regions, the seasonal snowpack contributes a major portion of the water budget. With a contribution of up to 50 % and more to the annual discharge, snow melt plays a key role in the dynamic of the hydrology of catchments of various high mountain areas such as the Himalayas (e.g., Jeelani et al., 2012), the Alps (e.g., Junghans et al., 2011) and the Norwegian mountains (e.g., Engelhardt et al., 2014), and is thus an equally important contributor to stream flow generation as rain in these affected areas. Furthermore, timing

and magnitude of the snow melt are major predictors for flood (Berghuijs et al., 2016) and land slide (Kawagoe et al., 2009) forecasts, and important factors in water resource management and operational hydropower forecasting. The extent and the temporal evolution of the snow cover is a controlling factor in the processes determining the growing-season of plants (Jonas et al., 2008). For all these reasons, a good representation of the seasonal snowpack in hydrological models is paramount.

5 However, there are large uncertainties in many variables specifying the temporal evolution of the snowpack, and the snow albedo is one of the most important among those due to the direct effect on the energy input to the snowpack from solar radiation. Fresh snow can have an albedo of over 0.9, reflecting most of the incoming solar radiation. However, the snow albedo undergoes strong variations: as snow ages, the snow grain size increases and albedo will drop as a result of the altered scattering properties of the larger snow grains. Furthermore, ambient conditions also play a large role. The ratio of diffuse and

10 direct incoming shortwave radiation, the zenith angle of the sun, and the albedo of the underlying ground in combination with the snow thickness can have a large impact on the snow albedo. Of recent significance is the role light absorbing impurities, or particles, which absorb in the range of the solar radiation, have on albedo when present in the snowpack (further called LAISI, light absorbing impurities in snow and ice). These LAISI originate mainly from fossil fuel combustion and forest fires (black carbon, BC) or from mineral dust or volcanic ash, and have species-specific radiative properties (Warren and Wiscombe, 1980).

15 With an understanding of the snow properties, the radiative properties of the LAISI, and the vertical distribution of the LAISI in the snowpack, the effect on the snow albedo can be simulated using a radiative transfer model for snow (Hadley and Kirchstetter, 2012). However, the fate of the LAISI once they are deposited on the snow are rather uncertain. Current theory indicates the absorbing effect of LAISI is most efficient when the LAISI reside at or close to the snow surface, and that subsequent snow fall burying the LAISI leads to a decline in or complete loss of the effect. However, as snow melts the

20 LAISI can reappear and retain near to the surface due to inefficient melt scavenging, which leads to an increase in the near surface concentration of LAISI and as such to a further decrease in the snow albedo, the so called melt amplification (e.g., Doherty et al., 2013). Field observations suggest that the magnitude of this effect is determined by the particle size and the hydrophobicity of the respective LAISI (Doherty et al., 2013). However, laboratory experiments investigating this effect are inexistent and field studies, rare. Conway et al. (1996) observed the vertical redistribution and the effect on the snow albedo by

25 adding volcanic ash and hydrophilic and hydrophobic BC to the snow surface of a natural snowpack. Flanner et al. (2007) used the results from Conway et al. to determine the scavenging ratios, specifying the ratio of BC contained in the melting snow that is flushed out with the melt water, of both hydrophilic and hydrophobic BC and used the results to simulate the radiative forcing of BC in snow on a global scale.

As LAISI lower the snow albedo, the effect on the snow melt has the potential to alter the hydrological characteristics of

30 catchments where snow melt significantly contributes to the water budget. Only a few studies developed model approaches to resolve the impact of LAISI on the snow melt discharge generation. Painter et al. (2010) showed that dust, transported from remote places to the Colorado river basin, can have severe implications on the hydrological regime due to disturbances to the discharge generation from snow melt during the spring time, shifting the peak runoff in spring by several weeks and leading to earlier snow free catchments and a decrease in annual runoff. The latter is mainly caused by earlier exposure of vegetation

35 and soils and a generally warmer snowpack and the subsequent increase in evapotranspiration. To date, hydrological models

investigating the impact of LAISI on the snow melt and runoff predominantly use empirical formulations to investigate the impact of LAISI on the radiative forcing in snow, by observing the net surface shortwave fluxes over snow and identifying the contribution from the LAISI through determination of the (hypothetical) clean snow albedo (e.g., Painter et al., 2007; Skiles et al., 2012). The development and use of those empirical relationships requires extensive field observations for model input

5 (e.g. the observed net surface shortwave fluxes over the snow surface). Due to the nature of the method (measuring the impacted variables and simulate the case without impact to achieve a measure for the impact), the consideration of the LAISI impact on the prediction of runoff in operational hydrological models as it is used for flood forecasting, water resource management and hydropower purposes is impractical when using this method. On the other hand, there is evidence that including the radiative forcing of LAISI in snow has the potential to further the quality of hydrological predictions: Bryant et al. (2013) showed that

10 during the melt period errors in the operational stream flow prediction of the National Weather Service Colorado Basin River Forecast Center are linearly related to dust radiative forcing in snow and concluded that implementing the effect of LAISI on the snow reflectivity could improve hydrological predictions in regions prone to deposition of light absorbing aerosols on snow. Furthermore, as we move more and more to physically composed hydrological models with a increasing complex abstraction of the physical processes involved in the evolution of the seasonal snowpack, factors that impact the snowpack evolution come

15 into the focus of interest that have been neglected before, such as the impact of LAISI on the snow albedo.

In this study we address this lack of knowledge by introducing a hydrological model with a newly developed snow algorithm that allows for a new class of forcing variables: the deposition rates of different species of light absorbing aerosols. Allowing for aerosol deposition, the algorithm uses a radiative transfer model for snow to account dynamically for the impact of the aerosols, or LAISI, on the albedo and the subsequent impacts on the snow melt and discharge generation. Aside from enabling

20 the user to optionally apply a deposition field, the algorithm depends on standard atmospheric forcing variables (precipitation, temperature, incoming short wave radiation, wind speed, and relative humidity).

We first present an overview over the hydrological model used in this study and the newly developed snow algorithm to treat LAISI in the snowpack in Sect. 2. To enable a critical evaluation of the newly developed snowpack algorithm, we conducted two independent analyses: i) a 1-D sensitivity study, and ii) a catchment scale of the impact of LAISI. A description of the

25 catchment used for our study and the forcing data sets is given in Sect. 3. Section 4 describes the 1-D model experiments and the model settings and calibration process in the case study. Lastly our results are presented together with the discussion distinctly for the model experiments first, followed by the case study within Sect. 5.

2 Modeling framework and the snowpack algorithm

In the following section we provide descriptions of the hydrologic model (Sect. 2.1) and the formulation of a novel snowpack

30 module used for the analyses (Sect. 2.2).

2.1 Hydrologic Model Framework

For the hydrological analysis we are using a hydrologic forecasting toolbox developed for hydropower forecasting by Statkraft (https://github.com/statkraft/shyft). The concept of Shyft follows the idea that a hydrological model can be expressed as a sequence of well known routines, each describing a certain aspect of the represented hydrological processes. Which processes are represented depend on the purpose of the model and the requirements of the user. The sequence of routines, the so called "methods-stack", is then run on a cell by cell basis, where the cell loosely represents an area of similar time-invariant geographical data (e.g. topographic properties or land type) with no specific restriction to cell geometry or area. According to the description above, Shyft is rather a model platform for hydrological purposes than a hydrological model. The Shyft framework allows for both following the paradigm of distributed, lumped parameter models, and more physically based approaches. It is not however, a fully coupled physically based model solving a system of differential equations. In every aspect it is optimized for highly efficient simulation of hydrological processes. The model-stack used herein consists of (i) a single-equation implementation to determine the potential evapotranspiration, (ii) a newly developed snowpack algorithm using an online radiative transfer solution for snow to account for the effect of LAISI on the snow albedo, and (iii) a first order nonlinear differential equation to calculate the catchment response to precipitation, snow melt and evapotranspiration. (i) and (iii) are described in more detail herein, while (ii) is described in detail in Sect. 2.2.

To determine the potential evapotranspiration, E_{pot}, we use the method according to Priestley and Taylor (1972)

$$E_{pot} = \frac{\alpha}{\lambda} \cdot \frac{s(T_a)}{s(T_a) + \gamma} \cdot R_n \tag{1}$$

with α = 1.26 being a dimensionless empirical multiplier, γ the psychrometric constant, $s(T_a)$ the slope of the relationship between the saturation vapour pressure and the temperature T_a, λ the latent heat of vaporization and R_n the net radiation.

The catchment response to precipitation and snow melt is determined using the approach of Kirchner (2009), who describes catchment discharge from a simple first order nonlinear differential equation. The underlying assumption of his approach is that the discharge is only a function of the liquid water in storage in the catchment, such that

$$Q = f(S) \tag{2}$$

where Q is the catchment discharge, S is the liquid water storage, and the $f(S)$ the functional relationship between Q and S, which is required to be reversible. Using the conservation-of-mass equation for a catchment,

$$\frac{dS}{dt} = P - E - Q \tag{3}$$

Kirchner (2009) finds the first order differential equation

$$\frac{dQ}{dt} = g(Q)(P - E - Q), \tag{4}$$

where $g(Q)$ (called the "sensitivity function") is the derivative with respect to S of the inverse of $f(S)$. $g(Q)$ can be estimated from the observed discharge alone for periods of the discharge time series for which the catchment precipitation (P) and

evapotranspiration (E) can be neglected. Kirchner (2009) uses the discharge time series of two catchments governed by humid climate and mild, snow poor winters (the Plynlimon catchments in mid-Wales; for more information see Robinson et al. (2013)) and recession plots to estimates $g(Q)$. He finds

$$ln(g(Q)) \approx c_1 + c_2 ln(q) + c_3 (ln(Q))^2 \tag{5}$$

with c_1, c_2 and c_3 being the only catchment specific parameters. To then solve Eq. (4) numerically using Eq. (5), Kirchner suggests to log-transform Eq. (4) due to a "smoother" profile of the log-transformed function:

$$\frac{d(ln(Q))}{dt} = \frac{1}{Q}\frac{dQ}{dt} = g(Q)(\frac{P-E}{Q} - 1) \tag{6}$$

In contrast to Kirchner's approach, we apply a slight adjustment. Firstly, we use the outflow response from the snow routine described in Sect. 2.2 instead of precipitation, P, to integrate Eq. (6). This outflow can be liquid precipitation, melt water, or a combination of both. In the catchments used by Kirchner (2009) "persistent snow cover is rare". For this reason, a contribution to the liquid water storage from snow melt is not considered in Eq. (3). Our study catchment is a high mountain catchment in Norway with a long lasting snow cover (typically until end of June; see Sect. 3). Thus, during spring and partly during summer, snow melt significantly contributes to the change in the liquid water storage, making the aforementioned adaptation necessary. Furthermore, the presence of a permanent snow layer and snow melt leads to a more challenging identification of periods when the change in liquid water storage is governed by discharge only.

Secondly, we assume that the sensitivity function, $g(Q)$, has the same form as described in Kirchner (2009) (see Eq. (5)) and estimate the parameters c_1, c_2 and c_3 by standard model calibration of simulated discharge against observed discharge using the Nash-Sutcliffe model efficiency as objective function, rather than using recession plots. Since we use a daily time step in our simulation, the identification of periods with negligible storage contribution from precipitation (and/or from snow melt) and evapotranspiration is reduced significantly compared to using an hourly time step: Kirchner (2009) uses an hourly time step and identifies predominantly rainless night hours, which satisfy the aforementioned condition.

As mentioned above, our main focus in this study lies on the representation of snow in the catchment and the impact of LAISI on the snow albedo, snow melt, and the subsequent effects on the catchment discharge. To account for the effect of light absorbing aerosols in the snow, we developed a new energy balance based snow accumulation and melt routine, described in the following section.

2.2 A new snowpack module for LAISI

The central addition provided in the algorithm described herein is the implementation of a radiative transfer solution to allow for the calculation of the snow albedo dynamically. This calculation allows a new class of forcing variables, wet and dry deposition rates of light absorbing aerosols, to be introduced, enabling the model to simulate the impact of dust, black carbon, volcanic ash or other aerosol deposition on snow albedo, snow melt and runoff. To account for the mass balance of LAISI in the snowpack while maintaining a representation of sub-grid snow variability and snow cover fraction (SCF), the energy balance

based snow algorithm underlies a tiling approach, where a grid-cell's snowfall is apportioned to sub-grid units following a gamma distribution.

In the following we present: (i) an overview of the energy balance calculations (Sect. 2.2.1), (ii) an introduction to the radiative transfer calculations required to represent LAISI in the snowpack (Sect. 2.2.2), and (iii) a new formulation for sub-gridscale tiling to represent snowpack spatial variability (Sect. 2.2.3).

2.2.1 Energy and mass budget

The energy budget of a snowpack can be expressed as:

$$\frac{\delta F}{\delta t} = K + L + H_s + H_l + R \tag{7}$$

with the net shortwave radiation flux K, the net longwave radiation flux L, the sensible and latent heat fluxes H_s and H_l, respectively, and the heat contribution from rain R (fluxes are considered to be positive when directed into the snowpack and as such an energy source to the snowpack). $\frac{\delta F}{\delta t}$ is the net energy flux into (or out of) the snowpack.

The net shortwave radiation is composed of the global radiation, K_{in}, and the reflected short wave radiation, K_{out}, and as such strongly dependent on the albedo, α.

$$K = K_{in} - K_{out} = K_{in}(1 - \alpha) \tag{8}$$

The model representation of the albedo α is subject of Sect. 2.2.2. The net longwave radiation is the difference between the incoming and outgoing longwave radiation and is usually expressed in terms of the Stefan-Boltzmann Law:

$$L = L_{in} - L_{out} = \epsilon_a \sigma T_a^4 - \epsilon_s \sigma T_s^4 \tag{9}$$

where ϵ_s and T_s are the emissivity and the surface temperature of the snow, respectively. In practical use T_a often refers to the air temperature (in units, K) measured at standard heights above the surface and ϵ_a is then called the effective clear sky emissivity of the atmosphere (e.g. Unsworth and Monteith (1975)). In our model approach, T_s is calculated as a function of the air temperature (T_a) rather than resolving heat conduction in multiple snow layers. Raleigh et al. (2013) found a high correlation between the air temperature measured at standard heights above the surface and T_s at various study sites with different characteristics. Following his finding, we assume a linear relationship between T_a and T_s:

$$T_s = m + n \cdot T_a \tag{10}$$

with free model parameters m and n. Hegdahl et al. (2016) used a similar approach with fixed parameters $m = -2.09$ and $n = 1.16$. Brutsaert (1975) present ϵ_a as a non-empirical simple function of the water vapour pressure e_a and T_a:

$$\epsilon_a = a \cdot (e_a/T_a)^b. \tag{11}$$

Sugita and Brutsaert (1992) used data from the First International Satellite Land Surface Climatology Project (ISLSCP) Field Experiment (FIFE) to determine the free parameters to $a = 0.980$ and $b = 0.0687$. Direct measurements of e_a are rather uncommon, but can be calculated via

$$e_a = e_s \cdot r_h \tag{12}$$

where e_s is the equilibrium water pressure and r_h is the relative humidity. The latter is a common variable measured at meteorological observation stations. An approximation for e_s over water and ice is given by Bosen (1960) and Bosen (1964).

Radiative exchanges dominate the snow melt rate in most snow melt scenarios. However, the fluxes of sensible and latent heat often contribute significantly due to vertical gradients in the air temperature and the vapour pressure. They are largely due to turbulent exchange processes and as such strongly dependent on the wind speed. The physically consistent determination of H_s and H_l over snow is rather difficult and requires complex instrumentation (e.g., Eddy Correlation Method). Various attempts have been made to ease the calculation (e.g., Gray and Male, 1981); we have followed Anderson (1976) and employ a bulk-transfer approach to approximate the turbulent fluxes of sensible and latent heat as functions of wind speed, temperature and air humidity, where the impact of the wind speed is represented in a linear, two-parametric wind-function. The parameters of the wind function (intercept and slope) are then determined by model calibration.

For the calculation of the heat contribution from rain R, we assume that rain falling on top of snow is cooled from atmospheric temperature T_a to the freezing temperature of water T_f, releasing the sensible heat

$$R = \rho_w c_w r (T_a - T_f) \tag{13}$$

where ρ_w and c_w are the density and heat capacity of water, respectively.

If Eq. (7) results in an energy surplus, we assume that the surplus is consumed by snow melt, expressed in snow water equivalent (SWE), less the change in the cold content of the top 30 mm of SWE of the snowpack.

2.2.2 Aerosols in the snowpack

Wiscombe and Warren (1980) and Warren and Wiscombe (1980) developed a robust and elegant model for snow albedo that remains today as a standard. Critical to their approach was the ability to account for: (i) wide variability in ice absorption with wavelength, (ii) the forward scattering of snow grains, and (iii) both diffuse and direct beam radiation at the surface. Furthermore, and of particular importance to the success of the approach, the model relies on observable parameters.

To solve for the effect of light absorption of LAISI in the snowpack on the snow albedo, we have integrated a two-layer adaption of the Snow, Ice, and Aerosol Radiative (SNICAR) model (Flanner et al., 2007, 2009) into the energy and mass budget calculations of Sect. 2.2.1. SNICAR utilizes the theory from Wiscombe and Warren (1980) and the two-stream, multilayer radiative approximation of Toon et al. (1989). Following Flanner et al. (2007), our implementation of SNICAR uses five

5 spectral bands (0.3–0.7, 0.7–1.0, 1.0–1.2, 1.2–1.5, and 1.5–5.0 um) in order to maintain computational efficiency, and individual broadband optical ice and aerosol properties were weighted by incident solar flux following the Chandrasekhar mean approach (Thomas and Stamnes, 1999). The incident flux were simulated offline assuming mid-latitude winter clear- and cloudy-sky conditions. Flanner et al. (2007) compared results from 5 bands scheme to the default 470 bands scheme in SNICAR and concluded that relative errors are less than 0.5%.

10 Both the albedo of clean snow and the effect of LAISI on the snow albedo strongly depend on the snow grain effective radius (or optical grain size) r. The snow grain effective radius r in turn alters as snow ages. To represent the effect of snow ageing on the evolution of the snow grain effective radius, we use a fast exponential limited growth for air temperatures above 0°C and a slow linear growth for air temperatures below or equal to 0°C:

$$
r_t = \begin{cases} r_{max} - (r_{max} - r_{t-1}) \cdot 2^{-\frac{1}{d_{fast}}\Delta t} & T_a > 0°\text{C} \\ r_{t-1} + \frac{1}{2}\frac{r_{max}-r_{min}}{d_{slow}}\Delta t & T_a \leq 0°\text{C} \end{cases}
\tag{14}
$$

15 with r_t and r_{t-1} being the snow grain effective radius at time t and $t-1$, respectively, r_{min} and r_{max} the snow grain effective radius of fresh and old snow, respectively, and d_{fast} and d_{slow} the fast and the slow growth rates, which are determined by model calibration.

In our snow algorithm, LAISI in snow are represented in two layers: (i) a surface layer with a time invariant maximum depth (in mm SWE), where the concentration of each LAISI species is calculated from a uniform mixing of the layer's snow with the

20 aerosol mass originating from atmospheric dry and wet deposition; and (ii) a bottom layer, representing the snow exceeding the maximum depth of the surface layer. We assume a mid-estimate layer thickness based on findings from Krinner et al. (2006), who assumes a maximal surface layer thickness of 8 mm SWE based on observation of 1 cm thick dirty layers in alpine firn cores used to identify summer horizons. Flanner et al. (2007) assumes a surface layer which doesn't exceed a maximum snow depth of 2 cm, which matches our approach when a density of melting snow of circa 400 kgm^{-3} is assumed. Since we expect

25 surface concentrations of LAISI in snow to be quite sensitive to the surface layer thickness of our model, we account for the uncertainty of the maximal surface layer thickness with a factor of 2.

We allow for LAISI fluxes between the two layers during snow accumulation and snow melt. During snow accumulation, LAISI are transferred from the surface to the bottom layer due to (partly) replacement of the surface snow by new snow. During this process, the total LAISI mass in the snow column is conserved. Under melt conditions, we allow for meltwater

30 scavenging. Simlar to Eq. (3) of Flanner et al. (2007), who generalized the representation of a snowpacks LAISI mass loss due

to meltwater scavenging of Jacobson (2004) for multiple snow layers, we characterize the magnitude of melt scavenging using the scavenging ratio k and calculate the temporal change of BC mass m_s in the surface layer as

$$\frac{dm_s}{dt} = -kq_sc_s + D,$$
(15)

and the change of BC mass m_b in the bottom layer as

$$\frac{dm_b}{dt} = k(q_sc_s - q_bc_b),$$
(16)

where q_s and q_b are the mass fluxes of melt water from the surface to the bottom layer and out of the bottom layer, respectively, and c_s and c_b are the mass mixing ratios of BC in the respective layer. A value for k of <1 is equal to a scavenging efficiency of less than 100% and hence allows for accumulation of LAISI in the surface layer. This effect is known as "melt amplification" and causes a further reduction of the albedo. In our model, we assume that melt water is mainly originating from the surface layer. We allow for melt from the bottom layer only when the potential melt per time step is exceeding the maximum depth of the surface layer (both in mm SWE).

To date, estimates of the scavenging ratio k are mostly based on experiments conducted by Conway et al. (1996). They treated a 2.5 cm deep surface layer of natural snow with different LAISI species (hydrophilic and hydrophobic soot and volcanic ash) during snow melt conditions and observed the effect on the albedo over time compared to natural snow and the vertical redistribution of the different LAISI species due to melt scavenging and surface accumulation. Flanner et al. (2007) used the results from Conway et al. (1996) to estimate the scavenging ratio of hydrophobic BC k_{phob} to 0.03, by applying and e-folding model with the melt water observed in a 10 days melt period and initial and final BC mass in the top 2 cm. Using the k_{phob}/k_{phil} ratio from analysis of observations in the top 50 cm of snow, he estimated k_{phil} to 0.2. To account for the uncertainty in the estimations, Flanner et al. (2007) used a order of magnitude variation on these estimates. These uncertainty might seem large, however, Flanner et al.'s calculations of the scavenging ratios of hydrophilic and hydrophobic BC are based on only one dataset (presented in Conway et al. (1996)), and accurate measurements that allow an uncertainty estimate of the scavenging don't exist to the knowledge of the authors. Doherty et al. (2013) suggest that the scavenging efficiency are determined by the total particle size and the hydrophobicity, rather than determined by the particle components. We only account for determination by hydrophobicity by distinguishing between hydrophobic and hydrophilic BC according to the type of deposition mechanism (hydrophilic BC from wet deposition, hydrophobic BC for dry deposition; see Sect. 3). Flanner et al. (2007) treats aged, hydrophilic BC as sulphate coated to account for the net increase in the mass absorption cross section (MAC) by 1.5 at λ=550 nm compared to hydrophobic BC caused by the ageing of BC (reducing effect on MAC) and particle coating from condensation of weakly absorbing compounds (enhancing effect on MAC) suggested by Bond et al. (2006). As a consequence, hydrophilic BC absorbs stronger than hydrophobic BC under the same conditions. On the other hand, hydrophilic BC underlies a more efficient melt scavenging. The competing mechanisms are subjects of the 1-D sensitivity study in Sect. 5.1.3.

2.2.3 Sub-grid variability in snow depth and snow cover

The representation of sub-grid snow variability can play a key role in modelling the hydrology of areas with a seasonal snow-pack (e.g., Hartmann et al., 1999). Several approaches exist to capture the sub-grid snow covered fraction (SCF) and distribution of snow water equivalent. Statistical approaches often use so called snow depletion curves to describe a relationship between a

5   prognostic snow variable (e.g snow water equivalent (SWE), accumulated melt depth) and regional observations of SCF, (e.g., Liston, 2004; Luce and Tarboton, 2004; Kolberg and Gottschalk, 2010). However, such approaches do not allow for explicit treatment of snow layers, which is required when simulating the concentrations of LAISI in snow. More physically based approaches aim to resolve the redistribution of snow with a dependence on topography and wind effects (e.g., Winstral and Marks, 2002). In our model, we further developed an approach assuming that the spatial distribution of each single event of

10   solid precipitation follows a certain probability distribution function. From this distribution we calculate multiplication factors, which then are used to assign the snowfall of a model grid cell to a number of subgrid computational elements, the so called tiles. Each of the tiles underlies independently from each other the snow algorithm described in Sect. 2.2, implying that variables related to the snow state, such as SWE, liquid water content, impurity content, and snow albedo; and the related contribution of long- and shortwave radiation fluxes to the energy balance, differ among the tiles. This also allows to simulate

15   the subgrid variability in impurity content. To calculate the multiplication factors, we follow the work of others (e.g., Kolberg and Gottschalk, 2010; Gisnås et al., 2016), and assume that the subgrid redistributed snow follows a gamma distribution, determined by the coefficient of variation (CV). CV values were derived based on work done by Gisnås et al. (2016), who used Winstral and Marks (2002)'s terrain-based parametrization to model snow redistribution in Norway by accounting for wind effects during the snow accumulation period over a digital elevation model with 10 m resolution. The redistribution model was

20   calibrated with snow depth data from Airborne Laser Scanning (ALS) over the Hardangervidda mountain plateau (see Melvold and Skaugen (2013)) and evaluated with snow depth data from ground penetrating radar observations at Finse, both located in Southern Norway. The detailed scheme is described in Gisnås et al. (2016). In the case study presented in Sect. 5.2, we use the CV values from Gisnås et al. (2016) to derive a linear relationship between the model cell's elevation and the corresponding CV value by simple linear regression (see left Fig.1), which results in a R^2-value of 0.71 and a p-value of smaller than 2.0e-5

25   for the study area. The linear relationship is only applied to cells with an areal forest cover fraction of lower than or equal to 0.5. For cells with a forest cover fraction of higher than 0.5, a constant snow CV value of 0.17 is used, following the findings of Liston (2004) for high latitude, mountainous forest. Examples of multiplication factors for forested cells and forest free cells in a reasonable range are shown in right Fig. 1.

3   Site description, meteorologic forcing and atmospheric deposition data

30   We selected the unregulated upper Atna catchment for our analysis. This catchment is located in a high elevation region of southern Norway (left Fig. 2). The watershed covers an area of 463 km^2 and ranges in elevation from 700 masl at the outlet at lake Atnsjoen to over 2000 masl in the Rondane mountains in the western part of the watershed (right Fig. 2), with approximately 90 % of the area above the forest limit. The average annual precipitation in the watershed during the study

period is approximately 655 mm, where most precipitation falls as rain in summer. The mean annual discharge is approximately 11 m^3s^{-1}, with low flows of 1-3 m^3s^{-1} during the winter months and peak flows of over 130 m^3s^{-1} during the spring melt season. For the 1-D sensitivity study of Sect. 5.1 we developed representative forcing data based on the conditions in this catchment.

5   For the meteorological forcing of precipitation, temperature, relative humidity and wind speed we use daily observations from the Norwegian Water Resources and Energy Directorate (NVE) and the Norwegian Meteorological Institute (MET). Four meteorological stations are located in the watershed at elevations between 701 and 780 masl along the Atna river, two of these measuring precipitation and two measuring temperature (see right Fig. 2). Observations of relative humidity and wind speed originate from two stations at locations close by the catchment (not shown in right Fig. 2). Further information about

10   the stations are given in Table 1. Due to poor availability of continuous solar radiation observations in Norway, we use for the forcing of global radiation gridded data from the Water and Global Change (WATCH) Forcing Data methodology applied to ERA-Interim reanalysis data (WFDEI; Weedon et al. (2014)) with a resolution of 0.5°. BC aerosol deposition rates over the catchment area are simulated using the regional aerosol-climate model REMO-HAM (described in more detail in Sect. 3.1). Discharge observations are from a station located at the outlet of the catchment at lake Atnsjoen and are used for model

15   calibration and validation.

3.1 Atmospheric deposition of black carbon from the REMO-HAM model

The wet and dry deposition rates of BC for the study area are generated using the regional aerosol-climate model REMO-HAM (Pietikäinen et al., 2012). For the simulations, we follow the approach of Hienola et al. (2013), but with changes to the emission inventory: Hienola et al. (2013) used emissions based on the AeroCom emission inventory for the year 2000 (see Dentener

20   et al., 2006). In the REMO-HAM simulations conducted herein, emissions are made by the International Institute for Applied Systems Analysis (IIASA) and are based on the Evaluating the Climate and Air Quality Impacts of Short-Lived Pollutants (ECLIPSE) V5a inventory for the years 2005, 2010, and 2015 (years in between were linearly interpolated) (Klimont et al., 2015b, a). We updated also other emissions modules (wildfire, aviation and shipping) following the approaches presented in Pietikäinen et al. (2015). The only difference to Pietikäinen et al. (2015) in this work is that we used the Global Fire Emissions

25   Database (GFED) version 4 based on an updated version of van der Werf et al. (2010).

REMO-HAM was used for the same European domain as in Pietikäinen et al. (2012) using 0.44° spatial resolution (50 km), 27 vertical levels and 3 minutes time step. The ERA-Interim re-analysis data was utilized at the lateral boundaries for meteorological forcing (Dee et al., 2011) and for the lateral aerosol forcing, data from the global aerosol-climate model ECHAM-HAMMOZ (version echam6.1.0-ham2.2) was used. ECHAM-HAMMOZ was simulated in a nudging mode, i.e. the model's

30   meteorology was forced to follow ERA-Interim data, and the ECLIPSE emissions were used (plus other updated emission modules shown in Pietikäinen et al. (2015)). The boundaries were updated every 6 hours for both meteorological and aerosol related variables. Simulations with REMO-HAM were conducted for the time period of 01.07.2004 - 31.12.2014 and the first three months were excluded from the analysis (spin-up period). The initial state for the model was taken from the boundary data, except for the soil parameters which were taken from a previous long-term simulation for the same domain (a so called

Hydrology and
Earth System
Sciences

Open Access

Discussions

EGU

warm-start). The output frequency of REMO-HAM was 3 hours and the total BC deposition flux was calculated from the accumulated dry and wet deposition and sedimentation fluxes.

In the snow algorithm used in this study, dry deposition and sedimentation are treated the same way. For simplicity, dry deposition will from now on be used to refer to the sum of REMO-HAM dry deposition and sedimentation.

4 Model experiments and calibration

Our analysis is in two parts in Sect. 5. First we present a 1-D sensitivity study investigating the impact of parameters and variables specific to the algorithm determining the effect of LAISI (Sect. 5.1). We then demonstrate the significance of BC in snow forcing on the catchment scale in a case study by simulating the impact of wet and dry deposition of BC in a remote south Norwegian catchment (Sect. 5.2).

We assume uncertainties of the LAISI forcing to originate mainly from the model representation of surface layer thickness impacts on the LAISI surface concentration and melt amplification due to inefficient melt scavenging, and uncertainties in the deposition forcing data. To account for the uncertainties, we declare minimum (min), central (mid), and maximum (max) effect estimates to each of the critical parameters, outlined in Table 2. The min, mid, and max estimates are both subjects of analysis in the sensitivity study (further described in Sect. 4.1) and used in the case study to give an uncertainty estimate of the LAISI effect on the hydrologic variables (further described in Sect. 4.2). We investigate the impact of BC impurities on the response variables by comparing the results from Aerosol Radiative Forcing model experiments ("ARF" scenarios) to simulations in which all BC deposition rates are set to zero ("no ARF" scenario).

4.1 1-D sensitivity study experiments

For the 1-D sensitivity study presented in Sect. 5.1, we use synthetic forcing data according to Table 3. The forcing data is divided into two periods, the snow accumulation period and the snow melt period, and held constant during each of the periods. The forcing applied during the snow accumulation period of 180 days results in 250 mm of SWE at the end of the accumulation period. This value is representative of the mean SWE of the upper 50% of tiles (factor Nr. 5 to 10 in right Fig. 1) at winter snow maximum in the Atnsjoen catchment during the study period of the case study. Deposition rates during the snow accumulation period were set to the average BC deposition rate during snow accumulation periods in the Atnsjoen catchment simulated with the regional aerosol-climate model REMO-HAM (see Sect. 3.1). After the snow accumulation period, we invoked a time invariant forcing to slowly melt the snowpack until meltout. The forcing applied for melt is based on the average forcing during the melt season from mid March until mid July of the Atnsjoen catchment and results in a melt period of ca. 25-35 days, depending on the scenario applied. This is in the range of the average time period it takes from snow maximum in a tile to meltout averaged over all snow tiles and melt seasons in the Atnsjoen catchment. For the melt period, different model setups are applied, investigating how the snowpack evolution depends on (i) the maximum surface layer thickness of the model (Sect. 5.1.1), (ii) the scavenging ratio of BC (Sect. 5.1.2), (iii) the BC species (hydrophobic or hydrophilic; Sect. 5.1.3) and (iv) the amount of snow at melt season start (Sect. 5.1.4). For simplicity and comparability reasons we assume during all 1-D

experiments except (iii) that only one species of BC is present in the snowpack (hydrophilic BC if not otherwise specified). The impact of the different model settings on the snowpack evolution under the influence of ARF is investigated by comparing the model results to equivalent simulations where ARF is not included. Specific model settings used in the experiments (i) to (iv) are described as follows:

4.1.1 Surface layer thickness

To investigate the impact of the maximum surface layer thickness of the model, we applied the synthetic forcing data to the snow algorithm using a maximal surface layer thickness of 4.0 mm SWE (maximum effect estimate in the case study of Sect. 4.2), 8.0 mm SWE (central effect estimate), 16.0 mm SWE (minimum effect estimate) and a maximal surface layer thickness that exceeds the total SWE of the snowpack at melt-onset. The last of which represents a single layer snow model with a vertically uniform distribution of LAISI as a bottom layer is only invoked in the model when the snowpack exceeds the maximum surface layer. We set the scavenging ratio of BC to 0.0 to isolate the effect of the surface layer thickness. This implies that during the melt period, the total mass of LAISI in the snowpack is conserved in all runs with ARF enabled. Results are shown in Sect. 5.1.1.

4.1.2 Scavenging ratio of BC

To analyse the sensitivity of the snowpack evolution during snow melt to the scavenging ratio used in the model, we evaluate separate scavenging parametrizations, but for single BC species. We chose to run the simulations with hydrophilic BC to separate the effect of melt scavenging ratio from species impacts (which is explored further in (iii)). We apply a range of values for the scavenging ratio: no melt scavenging (0.0; no melt scavenging), hydrophobic (0.03, mid estimate for hydrophobic BC in the case study of Sect. 4.2), hydrophilic (0.2; mid estimate for hydrophilic BC), and the upper estimate for hydrophilic BC (2.0; max estimate hydrophilic BC). While the scavenging ratios span values from hydrophobic to hydrophilic, by using only one species of BC (hydrophobic), we are able to isolate the effect of the scavenging ratio from absorption processes that are a function of the species. Results are shown in Sect. 5.1.2.

4.1.3 BC species

Hydrophilic BC absorbs stronger than hydrophobic BC under the same conditions due to an increased MAC compared to hydrophobic BC caused by the ageing of BC during atmospheric transport. On the other hand, hydrophilic BC undergoes more efficient melt scavenging. By applying the mid estimate of the scavenging ratio of hydrophobic BC (0.03) to both the hydrophobic BC and the hydrophilic BC we first investigate the isolated effect of the different absorption properties of the two species. We further apply the mid estimate for hydrophilic BC scavenging ratio (0.2) to hydrophilic BC to then quantify the gross effect. Results are shown in Sect. 5.1.3.

4.1.4 Impact of the amount of snow at melt onset

To isolate the impact of the amount of accumulated snow, we simulate the melting of snowpacks with the same total mass of LAISI uniformly distributed in the snow at melt onset, but with different SWE. Results are shown in Sect. 5.1.4.

4.2 Case study model setup and calibration

In the catchment scale simulations (Sect. 5.2), we investigate the impact of BC aerosol deposition on the catchment hydrology of a Norwegian catchment over a study period of 6 years, from September 2006 to September 2012. The station based forcing data described above is interpolated to the simulation cells (assumed to be 1x1 km^2 and accordingly smaller cells at the catchment boarders; right Fig. 2) using the Shyft internal interpolation algorithms. For temperature this implies Bayesian Kriging. For precipitation, BC deposition rates, wind speed and relative humidity this implies interpolation to the model cells via inverse distance weighting, with a constant vertical gradient applied for precipitation.

For model calibration, we first run a split sample calibration using the first 3 years (1 September 2006 to 31 October 2009) of the study period as calibration period and the following 3 years (1 September 2009 to 31 October 2012) for model validation. We choose the mid estimates (see Table 2) for all model parameters impacting the handling and effect of LAISI in the snowpack and aerosol depositions as simulated from REMO-HAM during model calibration. To asses the predictive efficiency of the model we use the Nash-Sutcliffe model efficiency (NSE)

$$NSE = 1 - \frac{\sum_{t=0}^{T}(Q_o^t - Q_s^t)^2}{\sum_{t=0}^{T}(Q_o^t - \overline{Q_o})^2} \tag{17}$$

where Q_o^t and Q_s^t are the observed and simulated discharge at time t, respectively, and $\overline{Q_0}$ is the mean observed discharge over the assessed period. To asses the uncertainty in the effect of LAISI on snow melt, we use the min and max effect estimates from Table 2, while holding constant all free model parameters as estimated during calibration. To assess the gross effect of LAISI we compare the simulations to equivalent simulations in which ARF is not included.

5 Results and Discussion

In the following, we first investigate the role of model parameters and variables critical to the effect of LAISI on the development of a melting snowpack by using the snow algorithm presented in Sect. 2.2 as point model (Sect. 5.1). We then examine the significance of the LAISI forcing for hydrological processes by simulating the impact of BC deposition on the snow melt and discharge generation in a snow dominated mountain catchment (Sect. 5.2).

5.1 1-D sensitivity studies

5.1.1 Sensitivity to surface layer thickness

We begin by examining the impact the maximum surface layer thickness of the model has on the LAISI induced snow melt implications. The central graph in Fig. 3a shows that the choice of the maximum surface layer strongly determines the increase in the surface concentration over the melt season - leading to a strong increase in surface BC until the end of the melt season with an increase in BC by a factor of circa 15, 30 and 60 for maximum layer thicknesses of 4.0, 8.0 and 16.0 mm, respectively, compared to the pre-melt season BC concentration. The thinner the surface layer is set, the stronger is the effect of BC on the albedo reduction and melt rate increase (see top graph in Fig. 3a), while the total aerosol mass is the same in all scenarios with ARF applied and constant over the melt season. When comparing the results of the three 2-layer scenarios (green, purple and red curves in column of graphs in Fig. 3a), one notices that even though the increase in surface layer concentration during the melt season differs strongly among the scenarios (center graph in Fig. 3a), the resulting difference on the albedo and melt rate (top graph in Fig. 3a) are relatively small; leading to a meltout of only slightly more than one and a half days between the scenario with the thickest and the thinnest surface layer setting.

The stronger increase in surface BC in model setups with thinner surface layer is due the inversely proportional relationship of the surface layer thickness with the increase in impurity concentration under the same mass flux of LAISI into the surface layer (from deposition or melt amplification): halving the surface layer thickness, leaving the mass flux of LAISI into the surface layer unchanged, leads to a doubling of the increase in the LAISI concentration and thus to differences in the vertical distribution of LAISI, with LAISI accumulated closer to the snow surface the thinner the surface layer is. Aerosol closer to the surface absorb more effectively due to the higher radiative intensity near the surface, which explains the stronger stronger albedo decrease and melt rate increase with thinner surface layer: the mean radiative intensity diminishes with depth due to absorption in snow and LAISI and scattering, leading to a less effective absorption of LAISI in deeper snow. By what means the radiative intensity diminishes with depth depends, among other variables, on the optical grain size of the snow. For example, in clean snow with an optical grain size of 50 um, the radiative intensity diminishes to $\frac{1}{e}$ of its surface value (the so called penetration depth) in 25.5 mm SWE. For snow with an optical grain size of 1000 um, the penetration depth increases to 117 mm SWE (both results from Flanner et al., 2007, assuming a wavelength of 550 nm and a solar zenith angle of 60°). For this reason, LAISI generally absorb more efficient in snow with a larger optical grain size. Thus, the differences in albedo and subsequent implications for melt of ARF scenarios compared to the no ARF scenario (black lines in Fig. 3a) are partly due to the increasing grain size during the melt period, and partly due to the accumulation of BC in the top layer. The relatively small differences in albedo, melt rate and snowpack development among the two-layer models (green, purple and red lines in top and bottom Fig. 3a) (despite the large differences in surface BC; central Fig. 3a), result from the fact that for all two-layer models, the surface layer thickness is much thinner than the penetration depth. Thus, LAISI in the surface layer absorb efficiently in all 2-layer scenarios and the difference in the albedo is relatively large compared to the no ARF scenario (solid black line in top graph of Fig. 3a), but relatively small among the two-layer scenarios (solid green, purple, and red line in top graph of Fig. 3a). This is a critical difference when a single layer model is used (solid yellow lines in Fig. 3a). With only one layer,

aerosol is distributed uniformly over the snowpack, and due to the scavenging ratio of 0.0, the total LAISI mass in the snow is conserved during the melt period. However, in contrast to the two-layer models, the LAISI concentration stays comparably low until shortly before meltout (solid yellow line in the center graph of Fig. 3a). Due to the uniform distribution of LAISI in the single layer model, a large fraction of the LAISI is located at depths where the radiative intensity is much lower than in the

5   top few mm of the snowpack, leading to a weaker absorption efficiency by the LAISI. This leads to a less pronounced lowering effect on the albedo in the beginning of the melt season compared to the two layer models (solid yellow line in the top graph of Fig. 3a) and thus to a shorter meltout shift (a bit less than five days; yellow line in bottom graph of Fig. 3a). Note that by simply adding a second layer, a doubling of the surface layer LAISI concentration occurs already when the accumulated melt equals the surface layer thickness, and thus the sensitivity to the deposition is enhanced; and arguably more representative of

10   real conditions.

The sensitivity study using different values for the maximum surface layer thickness provides three important results: First, when the properties of the LAISI considered in the simulation are prone to melt amplification (scavenging ration below 1), a minimum of two layers is required to simulate the effect due to potential accumulation of aerosol in the top layer. Second, for the effect on the albedo, it is more important that a surface layer is introduced rather than detailed knowledge about the

15   magnitude of the maximum surface layer, as long as the assumption that the surface layer thickness is much smaller than the penetration depth of the radiation into the snowpack is justifiable. Third, when introducing a surface layer, the surface concentration of the aerosol simulated strongly depends on the magnitude of the surface layer, which can make it difficult to compare with observations.

5.1.2   Sensitivity to scavenging ratio of BC

20   The results just presented for the simulations in Sect. 5.1.1 show the BC concentration increases by a factor of 15 to 60 during the melt period compared to the surface concentration at melt-onset (column of graphs in Fig. 3a). The strong increase in LAISI to the end of the season is largely dominated by the assumption that the total mass of LAISI is conserved during snow melt. In fact, field measurements indicate that a fraction of the aerosol is flushed out with the melt water, transported to deeper layers in the snowpack or completely flushed out with the melt water. In this section we explore the scavenging processes further.

25   Results are shown in the column of graphs of Fig. 3b. In the range of the applied scavenging ratios, we find a strong impact on the surface concentration of LAISI, the albedo, and the subsequent snow melt. When applying a melt scavenging factor typical for hydrophobic BC (green lines in graphs of Fig. 3b) there is little effect compared to the scenario without melt scavenging (purple lines; both show circa a factor 30 increase in surface BC concentration to the end of the melt season and only little differences in the development of albedo and snow melt). However, a distinction exists when using a scavenging

30   ratio estimate for hydrophilic BC. In contrast to the no melt scavenging and hydrophobic case, surface BC does not increase as rapidly through the simulation (red line, central graph of Fig. 3b) and in fact is completely flushed with the upper end of hydrophilic scavenging (yellow line).

The changes in the scavenging ratio do lead to a considerable effect on the albedo and the snow melt (meltout delayed by circa 1 (green lines), 2.5 (red lines), and 7 days (yellow lines) for scavenging ratios of 0.03, 0.2, and 2.0, respectively, compared

to no melt scavenging (purple lines in Fig. 3b)). Compared to the no ARF experiment (black lines), the presence of LAISI still causes an earlier meltout of circa 8, 6.5, and 2 days for scavenging ratios of 0.03, 0.2, and 2.0, respectively, in our simulation, implying a significant effect of BC on the albedo in all scenarios applied. Only when the melt scavenging is set to the upper limit (2.0; yellow lines in graphs of Fig. 3b), the surface concentration drops continuously during the melt period due to the

5 highly efficient melt scavenging. As a consequence, the albedo converges against the albedo of the no ARF case, before it drops roughly one day earlier to a value of circa 0.2 due to the earlier exposure of the underling ground (solid yellow and black line in top graph of Fig. 3b). The slight increasing in difference in the melt rate between the no ARF and the upper limit scavenging ratio scenario during the first 7 days from melt-onset are due to the increasing absorption efficiency of BC with increasing optical snow grain size, whereas the following convergence (day 7 until 17 from melt-onset) of both melt rates

10 are due to the decreasing LAISI concentration in the upper limit scavenging ration scenario due to ongoing removal of LAISI due to melt scavenging (compare the dashed yellow and black line in top graph of Fig. 3b). However, even though nearly all LAISI is removed from the snow by the end of the melt period in the upper limit scavenging ratio scenario, the melt out still happens circa two days earlier compared to the no ARF experiment, showing that small amounts of BC in snow can impact the snowpack evolution over the whole melt period even if it undergoes an efficient scavenging process.

15 ### 5.1.3   Sensitivity to BC species

Hydrophilic BC absorbs stronger than hydrophobic BC under the same conditions due to an increased MAC compared to hydrophobic BC caused by the ageing of BC during atmospheric transport. On the other hand, as we previously explored, hydrophilic BC undergoes more efficient melt scavenging. The column of graphs in Fig. 3c illustrates the net effect of these competing processes by applying the mid estimate of the scavenging ratio of hydrophobic BC (0.03) to both the hydrophobic

20 BC (green curve) and the hydrophilic BC (purple curves) species. In this manner these curves show the isolated effect of the different absorption properties of the two species. We further apply the mid estimate for hydrophilic BC scavenging ratio (0.2) to hydrophilic BC (red curves) to quantify the gross effect. As in other cases, we include the no ARF scenario (black curves) to highlight the overall effect on the albedo and melt of the different scenarios.

The isolated effect of the stronger absorption of hydrophilic BC leads to an earlier meltout by circa two days compared to

25 hydrophobic BC (purple and green curves in graphs of Fig. 3c). However, when applying the mid estimate of the scavenging ratio for hydrophilic BC (0.2), which we assume to be the most suited, the combined effects of stronger melt scavenging compared to hydrophobic BC leads to a masking of the isolated effect of stronger absorption by hydrophilic BC (and vice versa): during the melt period, the development of the snow albedo, melt rate and the snowpack SWE barely differ between the scenarios with the mid estimate scavenging ratios for hydrophobic and hydrophilic BC applied (red and green curves in top

30 and bottom graphs of Fig. 3c), showing that both scenarios, hydrophobic BC with low scavenging efficiency and hydrophilic BC with high scavenging efficiency, lead roughly to an earlier meltout by circa 6 days. We interpret this to indicate that it is more important to get the right total mass of BC deposition in the snowpack and the vertical distribution in the snow than it is to get the exact fraction between hydrophobic and hydrophilic BC in the model simulations.

5.1.4 Sensitivity to snowpack SWE at melt-onset

Fig. 4 shows the temporal shift to earlier melt out (in days) of snowpacks of different heights at melt-onset (in SWE) under the impact of ARF using different scavenging ratios compared to snowpacks where ARF is disregarded. Apart from the snow height and the scavenging ratio, all initial snowpack properties and the forcing data are kept constant, including the deposition

5 rate of BC during the accumulation period. This leads to snowpacks with the same total mass of BC and accordingly smaller concentrations at the start of the melt period. By doing so, we isolate the impact that the snowpack's SWE has on the effect of ARF in snow. With respect to the range of snowpack SWE at melt-onset presented here, the meltout shift shows an approximately linear relationship with SWE at melt-onset when all BC stays in the snowpack during melt (no melt scavenging included; solid line in Fig. 4). With a melt scavenging ratio in the range of the mid-estimates for hydrophilic and hydrophobic

10 BC, the BC effect on the melt out shift is similar to those where no scavenging was applied for small SWE at melt-onset, but the increase in the meltout shift gets less pronounced with increasing SWE at melt-onset (dashed and dashed-dotted curves in Fig. 4). When applying very efficient melt scavenging (dotted curve in Fig. 4), the effect on the meltout shift is rather small over the range of SWE values shown and converging against an upper limit.

The results suggest that not only the BC concentration and distribution, the snow properties, and the radiative properties and

15 hydrophobicity of the aerosol control how significantly BC in snow impacts the melt, but also the amount of snow accumulated: snowpacks with high concentrations of LAISI but little SWE are less impacted by the effect of LAISI on the snow melt than snowpacks with low concentrations of LAISI but high SWE. This difference is the more pronounced the less the LAISI are prone to melt scavenging. Transferred to the catchment scale, this means that snow rich catchments in general are more prone to be impacted by the deposition of light absorbing aerosols than catchments with medium or little snow accumulation during

20 winter under the influence of similar total LAISI mass input into the snowpack.

5.2 Case study: Impact of BC deposition on the hydrology of a south Norwegian catchment

5.2.1 Performance of the model

The model performs reasonably well during both calibration and validation, with NSEs of 0.86 during the calibration period (green line in Fig. 5a) and 0.82 during the validation period (red line in Fig. 5a). However, in all winter seasons except the

25 2010/2011 winter the model underestimates the winter discharge. This can also be seen in the scatter plot of simulated over observed discharge values for the whole simulation period shown in Fig. 6, which indicates an underestimation of low flow situations with flows between 0 and 15 $m^3 \, s^{-1}$. Furthermore, discharge peaks in the beginning of the melt season are commonly slightly underestimated. For conducting model experiments, we use model parameters estimated from a model calibration over the whole simulation period (1 September 2006 to 31 October 2012; Fig. 5b). Compared to the split sample calibration, the

30 parameters remain largely the unchanged, resulting in the same pattern of underestimating winter flow and spring discharge peaks. The NSE for the calibration over the whole period is 0.84.

Hydrology and
Earth System
Sciences
Discussions

Open Access

EGU

5.2.2 BC impact on catchment discharge and snow storage

Fig. 7a shows the simulated daily discharge and catchment SWE, averaged over the 6 years simulation period for the mid (red lines), min and max estimates (bounds of the shaded areas) and the scenario with BC depositions set to zero (no ARF scenario, black lines). The difference in daily discharge and catchment SWE of the min, mid and max scenarios to the no ARF scenario

5 are shown in Fig. 7b. All simulations with ARF applied show higher values in the daily discharge from end of March until end of May and lower discharge from end of may until mid August compared to the simulation without ARF applied. For the rest of the year, no effect on the discharge is noticeable. The total sum of daily discharge remains the same for all scenarios, implying that effects on the evapotranspiration due to a different evolution of the snow covered fraction (SCF) during spring are small and impacts on the cumulative discharge are not significant. This also implies that for the ARF scenarios higher

10 discharge early in the melt season and the lower discharge later in the melt season are counter-balancing on an annual scale and can be seen as a shift in the seasonal discharge pattern. Min, max and mid scenario all show the change from higher discharge to lower discharge compared to the no ARF scenario approximately at the same point of time (at the end of may; see blue marker in Fig. 7b). Because of this and since the applied ARF scenarios mostly have an impact on the magnitude of the effect on the discharge, but only little to no impact on the period when it acts enhancing or reducing, we can quantify the absolute

15 and relative effect on the discharge during the two periods. According to Fig. 7, ARF has on average an enhancing effect on the discharge generation from circa March 22 until May 29 and a reducing effect from May 30 until August 10. During the former (latter) period the average increase (decrease) in total discharge compared to the no ARF scenario is 0.20 (-0.18), 0.81 (-0.74) and 1.74 (-1.60) m^3 s^{-1} for the min, mid and max scenario, respectively. This relates to an average percentage increase in daily discharge of 2.5 %, 9.9 % and 21.4 % for the min, mid and max scenario from March 22 until May 29, respectively.

20 From May 30 until August 10, the decrease in discharge relates to a relative average change over the period of -0.8 %, -3.1 % and -6.7 %, respectively. Maximum increase in daily discharge during the 6 years simulation period is 1.4 m^3 s^{-1} (3.6 %), 5.6 m^3 s^{-1} (17.3 %), and 11.9 m^3 s^{-1} (42.7 %) for the min, mid and max estimates, respectively (not shown). The maximum decrease in daily discharge during the simulation is determined to -1.9 m^3 s^{-1} (-8.1 %), -8.2 m^3 s^{-1} (-11.4 %), -14.8 m^3 s^{-1} (-20.9 %) for the min, mid and max estimates, respectively (not shown).

25 In the following we refer to melt season as the period of time between March 22 and August 10. The differences in discharge among the scenarios can be explained with a differing evolution of the snowpack. The catchment SWE shown in Fig. 7a indicates large differences in the catchment averaged snowpack with a maximum during the second half of May, shortly before the surplus in discharge of the ARF scenarios compared to the no ARF scenario switches to the negative (see Fig. 7b). The average difference in catchment SWE of the min, mid and max scenario compared to the no ARF scenario during the melt

30 season is 1.5, 5.1 and 10.3 mm, which relates to an average decrease in SWE of 2.1 %, 7.4 % and 15.1 %, respectively. On average, the maximum difference in SWE is reached at the end of May and can be quantified with a relative decrease of the total amount of snow in the catchment of -4.6 %, -13.4 % and -34.4 % compared to the no ARF scenario at the respective point of time for the min, mid and max estimate. From June on, the differences in catchment SWE between the ARF and the no

Hydrology and
Earth System
Sciences

Discussions

Open Access

EGU

ARF scenarios drop continuously, which is equivalent to a higher catchment averaged snow melt rate in the no ARF scenario compared to the ARF scenarios.

An important contribution of evaluating the impact of ARF at the catchment scale is the expression of the dynamics of the hydrologic system. By including processes at the catchment scale, we find the increase in the difference during the beginning
5 of the melt season can be attributed to increased melt due to the effect of BC on the snow albedo. However, from end of May on we see a decrease in the differences in catchment SWE between the ARF and no ARF scenarios (Fig. 7b). By evaluating the impact of BC deposition at the catchment scale, we therefore expose the dynamics driven by the SCF of the catchment as a limiting factor to the catchment averaged snow melt.

This is more clear when looking at the development of the average snow albedo and the snow covered fraction (SCF) in the
10 catchment, shown in Fig. 8a. During the melt period, the catchment averaged albedo in all of the scenarios, decreases. We see the albedo of the max scenario having the largest drop and the one of the no ARF scenario being the lowest. Intuitively, one would expect more melting due to enhanced solar radiative forcing. However, we find that the differences in SWE between the scenarios from end of May on become less. The explanation is rather found when taking the development of the SCF into account. The SCF drops faster in the catchment when melt is increased due to ARF. This faster drop in SCF counteracts the
15 increased melt in the catchment driven by albedo. Hence, due to the area limitation from which snow can actually melt, the differences in SWE are then getting smaller, caused by the effect of smaller SCF on the catchment average melt overruling the effect of ARF.

The same as for the catchment SWE is valid for the discharge: the increased discharge of the ARF scenarios compared to the no ARF scenario during the beginning of the melt season can be attributed to increased melt due to the albedo effect of
20 BC on the snowpack, whereas the decreased discharge later in the season can be attributed to melt limitation caused by the simultaneous effect of the former increased melt on the SCF retreat.

5.2.3 Evolution of surface BC concentration and BC impact on snow albedo

During the snow accumulation period (circa until end of March), only little differences in albedo between the different model experiments are noticeable: the average annual snow albedo from January 1st until March 22nd is 0.871 for the no ARF
25 experiment (Fig. 8a). During the same time period, min, mid, and max experiments show albedo reductions of 0.003, 0.010, and 0.014 compared to the no ARF value, which can be interpreted as the pre-melt season effect of BC on the snow albedo. The differences in snow albedo between the ARF experiments during the pre-melt season are mostly due to the difference in the deposition scenario (factor 0.5 and 1.5 on the deposition of the min and the max scenario), and due to the setting of the maximum surface layer extent of the snowpack, leading to average surface layer concentrations of 12, 49 and 98 ng g^{-1}
30 (Fig. 8b) at the beginning of the melt period. With the start of the melt season, the difference in albedo gets larger between the different model experiments. This has several combined reasons: (i) with increasing grain size during the melt season, the absorbing effect of BC gets more efficient due to deeper penetration of radiation into the snowpack (snow of larger grains has a larger extinction coefficient and more effective forward scattering properties (Flanner et al., 2007)). This leads to a stronger effect of the pre-melt season BC concentrations on the albedo. (ii) With the start of the melt season and thus widespread retreat

of the vertical snow extent, BC can accumulate in the surface layer. This effect is strongly depended on the applied scavenging ratios of hydrophilic and hydrophobic BC as we demonstrated in the 1-D sensitivity study in Sect. 5.1. The magnitude of the scavenging ratio determines if BC can accumulate in the surface layer and acts to decrease on the albedo (scavenging ratio below 1) or if BC is efficiently removed by melt water, leading (as isolated effect) to an increase of albedo (scavenging ratio

5 above 1). The applied scavenging ratios of hydrophobic and hydrophilic BC in the mid (0.03 and 0.2, respectively) and max (0.003 and 0.02, respectively) model experiments are below 1 and accumulation of BC in the surface layer results. For the mid scenario, the spatially averaged surface BC increases from a pre-melt season value of about 49 ng g^{-1} to a surface BC concentration of circa 250 ng g^{-1} (factor 5 increase) to the end of the melt season (beginning of July). For the max experiment, the simulated surface BC concentration increases from roughly 100 ng g^{-1} to over 2500 ng g^{-1} (factor 25 increase). For the

10 min scenario the scavenging ratio for hydrophilic BC is 2.0 - leading to a decrease in the surface concentration of hydrophilic BC. Even though the surface concentration of hydrophobic BC increases, the total surface concentration of BC decreases due to the higher - circa factor 20 - hydrophilic BC concentration to the beginning of the melt season compared to the surface concentration of hydrophobic BC (see lower boundary of the shaded area in Fig. 8b). (iii) A third reason for the enhanced albedo is the strong increase in BC at the end of the melt season. The sub-grid snow variability plays an important role due

15 to the fact that BC is predominately wet deposited. The mid and max scenario show a roughly linear increase of surface BC concentration on a log-scale during the melt season. The tiles bearing little snow melt out more quickly than the tiles containing large snow accumulation. At the same time, tiles bearing large quantities of snow tend to also bear large quantities of BC (in terms of total BC mass) due to the dominantly wet-depositioned BC, which we chose in the model to follow the same redistribution as snow. Only dry deposition is assumed to deposit spatially homogeneous over the sub grid tiles. Late in

20 the melt season, the snow albedo is predominantly computed from tiles, that due to a high accumulation factor, were rich in snow after the snow accumulation period, and thus rich in BC mass. That leads to high accumulation in the top layer when combined with a scavenging ratio of below 1. This effect amplifies the catchment averaged surface BC concentration increase during the melt season in the mid and max estimate scenarios and contributes to the large differences in surface BC among the three scenarios to the end of the melt season. This large difference in surface BC between the different scenarios is then causing

25 the wide spread in snow albedo to the end of the melt season, lowering the average snow albedo in the catchment by about 0.03, 0.1 and over 0.3 in the min, mid and max estimate scenarios to the end of the melt season due to ARF. Qualitatively, we feel this represents reality well, in that if we think about snow patches in a catchment at the end of the season, they tend to be 'dirty', as the concentration of impurities increases while the water melts away.

The range of the catchment mean surface BC concentrations in the min, mid and max estimate becomes extremely high to the

30 end of the melt period, ranging over more than 3 orders of magnitude between the min and max estimate of the simulations (see Fig. 8b). However, at the point of time when these extreme differences are reached, the SCF of the catchment of all scenarios is converging toward zero - making the concentrations to this point of time not representative for the development throughout the melt period. But, on the other hand, the extreme diverging results highlight the high uncertainty that comes with simulation of the fate of LAISI in the snowpack and the ARF they are causing.

A significant challenge when evaluating these results is the severe lack of observations - not only in the catchment used herein as case study, but in general when simulating the impact of LAISI on the snowpack over a melt season - especially when the approach involves the determination of the LAISI concentrations in the snowpack from aerosol deposition rates. In the study on the global impact of the radiative forcing of BC in snow, Flanner et al. (2007) compare the model results with

5 various measurement of surface BC, representing many cryospheric regions of the globe - with overall good agreement with observations. For south Norway, Flanner et al. (2007) predict central estimate annual mean surface BC concentrations between 46 and 215 ng g^{-1} for the year 1998. Our simulations show concentrations in the range of Flanner et al. (2007)'s results (71 ng g^{-1} for the mid estimate average annual surface BC concentration over the 6 years period, and 18 and 198 ng g^{-1} for the min and max estimate, respectively). Our results further agree with the range of surface BC observations in mainland

10 Norway presented in Forsström et al. (2013).

Our model further suggests that melt amplification can have severe implications on the impact of LAISI on both, the snowpack evolution and the discharge regime of a catchment, which means that the seasonal cycle of surface BC concentration is of great importance. Especially for the impact on the hydrological cycle, the fate of the LAISI in melting snow is essential - which leads to great importance of surface BC concentrations during spring. The increase of the mid estimate surface BC

15 during the melt season agree with observations from Doherty et al. (2013), who measured a roughly 5 times increase in surface BC of a melting snow. The experiments conducted by Conway et al. (1996) investigating artificially added BC and on melting snow show similar results. Forsström et al. (2013) associates large spikes in observed surface BC with with snow melt, which supports the course of the mean surface BC concentration in the catchment resulting from the mid estimate simulation.

However, the surface BC concentrations during spring melt are also the most uncertain (see differing course of BC surface

20 concentration of min, mid and max estimate in Fig. 8b): the parameters quantifying the effect of melt amplification are are based on the results of a sole field experiment campaign only (namely the experiments conducted by Conway et al. (1996)). This relatively weak basis for the mid estimates of the model parameters, combined with lacking observational data of surface BC in our study region during the melt season leads then to the high uncertainties our model results are showing.

5.2.4 BC induced radiative forcing in snow and catchment

25 Fig. 9a shows the daily mean radiative forcing in the catchment snow induced by the presence of BC in snow averaged over snow bearing tiles only (herein after referred to as RFS, radiative forcing in snow). The RFS represents the additional uptake of energy from solar radiation due to the presence of BC in the snow compared to clean snow with the same properties. Our simulations suggest that the RFS underlies a strong annual cycle with low values during the snow accumulation period and steadily increasing values during spring snow melt, reaching values of approximately 8, 18 and 57 Wm^{-2} for the min, mid,

30 and max effect estimates, respectively, to the end of the spring melt season (see red solid line and shaded area in Fig. 9a). The strong increase in RFS during spring melt results from two combined processes: (i) the decrease in snow albedo due to the catchment wide increase in surface BC concentrations (melt amplification) and the increasing optical grain size in melting snow as discussed in Sect. 5.2.3 and (ii) the increasing daily solar irradiation due to a lower solar zenith angle and longer days. The RFS averaged over the 6 years simulation period is 0.50, 1.48 and 2.43 Wm^{-2} for the min, mid, max scenarios, respectively.

However, for the effect on the discharge generation, a more relevant variable is the SCF normalized daily radiative forcing in snow. As the SCF drops, the effect of the RFS on the melt generation in the catchment gets limited by the increasing area of bare ground. The net effect is shown in Fig. 9b, where the radiative forcing is normalized with the SCF. The results can be seen as a measure for the catchment wide additional energy uptake due to the presence of BC in snow, which on average reaches a maximum of 1.3, 4.9 and 8.8 Wm^{-2} (min, mid and max scenario, respectively) in around the beginning of May.

6 Conclusions

Herein we presented a newly developed snow algorithm for application in hydrologic models that allows a new class of forcing variables: the deposition rates of light absorbing aerosols. By coupling a radiative transfer model for snow to an energy balance based snowpack model, we are providing a tool that can be used to determine the effect of various species of LAISI on the hydrologic cycle on a catchment scale. From a 1-D model study, presented in Sect. 5.1, we conclude that:

i - the implementation of at least two layers (a thin surface layer and a bottom layer) is of outstanding importance to capture the potential effect of melt amplification on the near surface LAISI evolution. The maximum thickness (in SWE) of the surface layer herein has rather little effect on the snow albedo and melt rate as long as the maximum layer thickness is sufficiently small. However, the evolution of the LAISI surface concentration is highly sensitive to the choice of the surface layer extent.

ii - The determination on how LAISI is washed out of the snowpack with melt water has great effect on the evolution of LAISI concentration near the surface, snow albedo and melt rate. Due to rare observations of this effect the uncertainties are high and our findings show the need for more detailed understanding of the processes involved due to the high importance for the overall effect of LAISI in the snowpack.

iii - Snow rich catchments are more prone to be affected by LAISI than snow poor catchments when affected by similar deposition rates.

To prove the significance of the forcing from LAISI for the hydrologic cycle on a catchment scale we demonstrated the effect of BC deposition and the subsequent implications for snow melt and discharge generation due to impacts on the snow albedo on a remote mountain catchment. Even though our model approach is conservative due the lacking implementation of the effect of LAISI on the grain size growth and due to the choice of a remote northern catchment of only medium snow accumulation (compared to other Norwegian mountain catchments), we could show that the effect on the discharge generation is significant, even in low deposition regions like Norway, leading to a shift in the annual water balance. We conclude from this that our study shows the potential improvement of hydrologic modelling by including the effect of LAISI, especially when the model approach implicates a physically based representation of the snowpack in general and the snow albedo in particular.

Hydrology and Earth System Sciences

Discussions

Open Access

EGU

References

Anderson, E. A.: A Point Energy and Mass Balance Model of a Snow Cover, NOAA Technical Report NWS, 19, 1976.

Berghuijs, W. R., Woods, R. A., Hutton, C. J., and Sivapalan, M.: Dominant flood generating mechanisms across the United States, Geophysical Research Letters, 43, 4382–4390, doi:10.1002/2016GL068070, 2016.

5 Bond, T. C., Habib, G., and Bergstrom, R. W.: Limitations in the enhancement of visible light absorption due to mixing state, Journal of Geophysical Research, 111, D20 211, doi:10.1029/2006JD007315, 2006.

Bosen, J. F.: A formula for approximation of the saturation vapor pressure over water, Monthly Weather Review, pp. 275–276, 1960.

Bosen, J. F.: Formula for approximation of the ratio of the saturation vapor pressure over ice to that over water at the same temperature, Monthly Weather Review, 92, 508, 1964.

10 Brutsaert, W.: On a Derivable Formula for Long-Wave Radiation From Clear Skies, Water Resources Research, 11, 742–744, 1975.

Bryant, A. C., Painter, T. H., Deems, J. S., and Bender, S. M.: Impact of dust radiative forcing in snow on accuracy of operational runoff prediction in the Upper Colorado River Basin, Geophysical Research Letters, 40, 3945–3949, doi:10.1002/grl.50773, 2013.

Conway, H., Gades, A., and Raymond, C. F.: Albedo of dirty snow during conditions of melt, Water Resources Research, 32, 1713–1718, 1996.

15 Dee, D. P., Uppala, S. M., Simmons, A. J., Berrisford, P., Poli, P., Kobayashi, S., Andrae, U., Balmaseda, M. A., Balsamo, G., Bauer, P., Bechtold, P., Beljaars, A. C. M., van de Berg, L., Bidlot, J., Bormann, N., Delsol, C., Dragani, R., Fuentes, M., Geer, A. J., Haimberger, L., Healy, S. B., Hersbach, H., Hólm, E. V., Isaksen, L., Kållberg, P., Köhler, M., Matricardi, M., McNally, A. P., Monge-Sanz, B. M., Morcrette, J.-J., Park, B.-K., Peubey, C., de Rosnay, P., Tavolato, C., Thépaut, J.-N., and Vitart, F.: The ERA-Interim reanalysis: configuration and performance of the data assimilation system, Quarterly Journal of the Royal Meteorological Society, 137, 553–597, 20 doi:10.1002/qj.828, http://dx.doi.org/10.1002/qj.828, 2011.

Dentener, F., Kinne, S., Bond, T., Boucher, O., Cofala, J., Generoso, S., Ginoux, P., Gong, S., Hoelzemann, J. J., Ito, A., Marelli, L., Penner, J. E., Putaud, J.-P., Textor, C., Schulz, M., van der Werf, G. R., and Wilson, J.: Emissions of primary aerosol and precursor gases in the years 2000 and 1750 prescribed data-sets for AeroCom, 6, 4321–4344, doi:10.1029/2003JD003697,, 2006.

Doherty, S. J., Grenfell, T. C., Forsström, S., Hegg, D. L., Brandt, R. E., and Warren, S. G.: Observed vertical redistribution of black 25 carbon and other insoluble light-absorbing particles in melting snow, Journal of Geophysical Research: Atmospheres, 118, 5553–5569, doi:10.1002/jgrd.50235, 2013.

Engelhardt, M., Schuler, T. V., and Andreassen, L. M.: Contribution of snow and glacier melt to discharge for highly glacierised catchments in Norway, Hydrology and Earth System Sciences, 18, 511–523, doi:10.5194/hess-18-511-2014, 2014.

Flanner, M. G., Zender, C. S., Randerson, J. T., and Rasch, P. J.: Present-day climate forcing and response from black carbon in snow, Journal 30 of Geophysical Research: Atmospheres, 112, D11 202, doi:10.1029/2006JD008003, 2007.

Flanner, M. G., Zender, C. S., Hess, P. G., Mahowald, N. M., Painter, T. H., Ramanathan, V., and Rasch, P. J.: Springtime warming and reduced snow cover from carbonaceous particles, Atmospheric Chemistry and Physics, 9, 2481– 2497, doi:10.1029/2005JD006356,, 2009.

Forsström, S., Isaksson, E., Skeie, R. B., Ström, J., Pedersen, C. A., Hudson, S. R., Berntsen, T. K., Lihavainen, H., Godtliebsen, F., and Gerland, S.: Elemental carbon measurements in European Arctic snow packs, Journal of Geophysical Research: Atmospheres, 118, 13,614– 35 13,627, doi:10.1002/2013JD019886, 2013.

Gisnås, K., Westermann, S., Schuler, T. V., Melvold, K., and Etzelmüller, B.: Small-scale variation of snow in a regional permafrost model, The Cryosphere, 10, 1201–1215, doi:10.5194/tc-10-1201-2016, 2016.

Gray, D. M. and Male, D. H.: Handbook of Snow: Principles, Processes, Management and Use, Paperback, 1981.

Hadley, O. L. and Kirchstetter, T. W.: Black-carbon reduction of snow albedo, Nature Climate Change, 2, 437–440, doi:10.1038/NCLIMATE1433, 2012.

Hartmann, M. D., Baron, J. S., Lammers, R. B., Cline, D. W., Band, L. E., Liston, G. E., and Tague, C.: Simulations of snow distribution and hydrology in a mountain basin, 35, 1587–1603, 1999.

Hegdahl, T. J., Tallaksen, L. M., Engeland, K., Burkhart, J. F., and Xu, C.-Y.: Discharge sensitivity to snowmelt parameterization: a case study for Upper Beas basin in Himachal Pradesh, India, Hydrology Research, 47, 683–700, doi:10.2166/nh.2016.047, 2016.

Hienola, A. I., Pietikäinen, J.-P., Jacob, D., Pozdun, R., Petäjä, T., Hyvärinen, A.-P., Sogacheva, L., Kerminen, V.-M., Kulmala, M., and Laaksonen, A.: Black carbon concentration and deposition estimations in Finland by the regional aerosol–climate model REMO-HAM, Atmospheric Chemistry and Physics, 13, 4033–4055, doi:10.5194/acp-13-4033-2013, 2013.

Jacobson, M. Z.: Climate response of fossil fuel and biofuel soot, accounting for soot's feedback to snow and sea ice albedo and emissivity, Journal of Geophysical Research: Atmospheres, 109, n/a–n/a, doi:10.1029/2004JD004945, 2004.

Jeelani, G., Feddema, J. J., van der Veen, C. J., and Stearns, L.: Role of snow and glacier melt in controlling river hydrology in Liddar watershed (western Himalaya) under current and future climate, Water Resources Research, 48, n/a–n/a, doi:10.1029/2011WR011590, 2012.

Jonas, T., Rixen, C., Sturm, M., and Stoeckli, V.: How alpine plant growth is linked to snow cover and climate variability, Journal of Geophysical Research, 113, G03 013, doi:10.1029/2007JG000680, 2008.

Junghans, N., Cullmann, J., and Huss, M.: Evaluating the effect of snow and ice melt in an Alpine headwater catchment and further downstream in the River Rhine, Hydrological Sciences Journal, 56, 981–993, doi:10.1080/02626667.2011.595372, 2011.

Kawagoe, S., Kazama, S., and Ranjan Sarukkalige, P.: Assessment of snowmelt triggered landslide hazard and risk in Japan, Cold Regions Science and Technology, 58, 120–129, doi:10.1016/j.coldregions.2009.05.004, 2009.

Kirchner, J. W.: Catchments as simple dynamical systems: Catchment characterization, rainfall-runoff modeling, and doing hydrology backward, Water Resources Research, 45, n/a–n/a, doi:10.1029/2008WR006912, 2009.

Klimont, Z., Höglund-Isaksson, L., Heyes, C., Rafaj, P., Schöpp, W., Cofala, J., Borken-Kleefeld, J., Purohit, P., Kupiainen, K., Winiwarter, W., Amann, M., Zhao, B., Wang, S., Bertok, I., and Sander, R.: Global scenarios of air pollutants and methane: 1990-2050, In preparation, 2015a.

Klimont, Z., Kupiainen, K., Heyes, C., Purohit, P., Cofala, J., Rafaj, P., Borken-Kleefeld, J., and Schoepp, W.: Global anthropogenic emissions of particulate matter, In preparation, 2015b.

Kolberg, S. and Gottschalk, L.: Interannual stability of grid cell snow depletion curves as estimated from MODIS images, Water Resources Research, 46, n/a–n/a, doi:10.1029/2008WR007617, 2010.

Krinner, G., Boucher, O., and Balkanski, Y.: Ice-free glacial northern Asia due to dust deposition on snow, Climate Dynamics, 27, 613–625, doi:10.1007/s00382-006-0159-z, 2006.

Liston, G. E.: Representing Subgrid Snow Cover Heterogeneities in Regional and Global Models, Journal of Climate, 17, 1381–1397, 2004.

Luce, C. H. and Tarboton, D. G.: The application of depletion curves for parameterization of subgrid variability of snow, Hydrological Processes, 18, 1409–1422, doi:10.1002/hyp.1420, 2004.

Melvold, K. and Skaugen, T.: Multiscale spatial variability of lidar-derived and modeled snow depth on Hardangervidda, Norway, Annals of Glaciology, 54, 273–281, doi:10.3189/2013AoG62A161, 2013.

Painter, T. H., Barrett, A. P., Landry, C. C., Neff, J. C., Cassidy, M. P., Lawrence, C. R., McBride, K. E., and Farmer, G. L.: Impact of disturbed desert soils on duration of mountain snow cover, Geophysical Research Letters, 34, L12 502, doi:10.1029/2007GL030284, 2007.

Painter, T. H., Deems, J. S., Belnap, J., Hamlet, A. F., Landry, C. C., and Udall, B.: Response of Colorado River runoff to dust radiative forcing in snow, 107, 17 125–17 130, doi:10.1073/pnas.0913139107/-/DCSupplemental, 2010.

5 Pietikäinen, J.-P., Kupiainen, K., Klimont, Z., Makkonen, R., Korhonen, H., Karinkanta, R., Hyvärinen, A.-P., Karvosenoja, N., Laaksonen, A., Lihavainen, H., and Kerminen, V.-M.: Impacts of emission reductions on aerosol radiative effects, Atmospheric Chemistry and Physics, 15, 5501–5519, doi:10.5194/acp-15-5501-2015, http://www.atmos-chem-phys.net/15/5501/2015/, 2015.

Pietikäinen, J.-P., O'Donnell, D., Teichmann, C., Karstens, U., Pfeifer, S., Kazil, J., Podzun, R., Fiedler, S., Kokkola, H., Birmili, W., O'Dowd, C., Baltensperger, U., Weingartner, E., Gehrig, R., Spindler, G., Kulmala, M., Feichter, J., Jacob, D., and Laaksonen, A.: The regional

10 aerosol-climate model REMO-HAM, Geoscientific Model Development, 5, 1323–1339, doi:10.5194/gmd-5-1323-2012, 2012.

Priestley, C. H. B. and Taylor, R. J.: On the assessment of surface heat flux and evaporation using large-scale parameters, 100, 81–92, 1972.

Raleigh, M. S., Landry, C. C., Hayashi, M., Quinton, W. L., and Lundquist, J. D.: Approximating snow surface temperature from standard temperature and humidity data: New possibilities for snow model and remote sensing evaluation, Water Resources Research, 49, 8053–8069, doi:10.1002/2013WR013958, 2013.

15 Robinson, M., Rodda, J. C., and Sutcliffe, J. V.: Long-term environmental monitoring in the UK: origins and achievements of the Plynlimon catchment study, Transactions of the Institute of British Geographers, 38, 451–463, doi:10.1111/j.1475-5661.2012.00534.x, 2013.

Skiles, S. M., Painter, T. H., Deems, J. S., Bryant, A. C., and Landry, C. C.: Dust radiative forcing in snow of the Upper Colorado River Basin: 2. Interannual variability in radiative forcing and snowmelt rates, Water Resources Research, 48, W07 522, doi:10.1029/2012WR011986, 2012.

20 Sugita, M. and Brutsaert, W.: Cloud Effect in the Estimation of Instantaneous Downward Longwave Radiation, Water Resources Research, 29, 599–605, doi:10.1029/92, 1992.

Thomas, G. E. and Stamnes, K.: Radiative Transfer in the Atmosphere and Ocean, Cambridge University Press, doi:10.1017/CBO9780511613470, 1999.

Toon, O. B., Mckay, C. P., and Ackerman, T. P.: Rapid Calculation of Radiative Heating Rates and Photodissociation Rates in Inhomogeneous

25 Multiple Scattering Atmospheres, 94, 16,287–16,301, 1989.

Unsworth, M. H. and Monteith, J. L.: Long-wave radiation at the ground I. Angular distribution of incoming radiation, 101, 13–24, doi:10.1002/qj.49710142703, 1975.

van der Werf, G. R., Randerson, J. T., Giglio, L., Collatz, G. J., Mu, M., Kasibhatla, P. S., Morton, D. C., DeFries, R. S., Jin, Y., and van Leeuwen, T. T.: Global fire emissions and the contribution of deforestation, savanna, forest, agricultural, and peat fires (1997-2009),

30 Atmospheric Chemistry and Physics, 10, 11 707–11 735, doi:10.5194/acp-10-11707-2010, http://www.atmos-chem-phys.net/10/11707/2010/, 2010.

Warren, S. G. and Wiscombe, W. J.: A Model for the Spectral Albedo of Snow. II: Snow Containing Atmospheric Aerosols, Journal of the Atmospheric Sciences, 37, 2734–2745, 1980.

Weedon, G. P., Balsamo, G., Bellouin, N., Gomes, S., Best, M. J., and Viterbo, P.: The WFDEI meteorological forcing data set: WATCH Forc-

35 ing Data methodology applied to ERA-Interim reanalysis data, Water Resources Research, 50, 7505–7514, doi:10.1002/2014WR015638, 2014.

Winstral, A. and Marks, D.: Simulating wind fields and snow redistribution using terrain-based parameters to model snow accumulation and melt over a semi-arid mountain catchment, Hydrological Processes, 16, 3585–3603, doi:10.1002/hyp.1238, 2002.

Wiscombe, W. J. and Warren, S. G.: A Model for the Spectral Albedo of Snow. I: Pure Snow, Journal of the Atmospheric Sciences, 37,
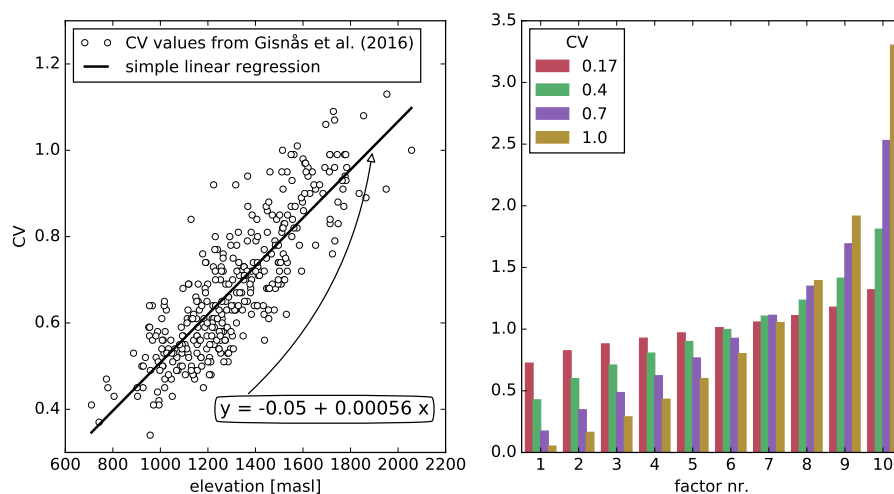2712–2733, 1980.

Figure 1. Left: coefficients of variation (CV) from Gisnås et al. (2016) of forest free areas in the Atnsjoen catchment (red dots) and the relationship between the CVs and the elevation resulting from simple linear regression analysis (black line). Right: solid precipitation multiplication factors for the snow tiles for different CVs.
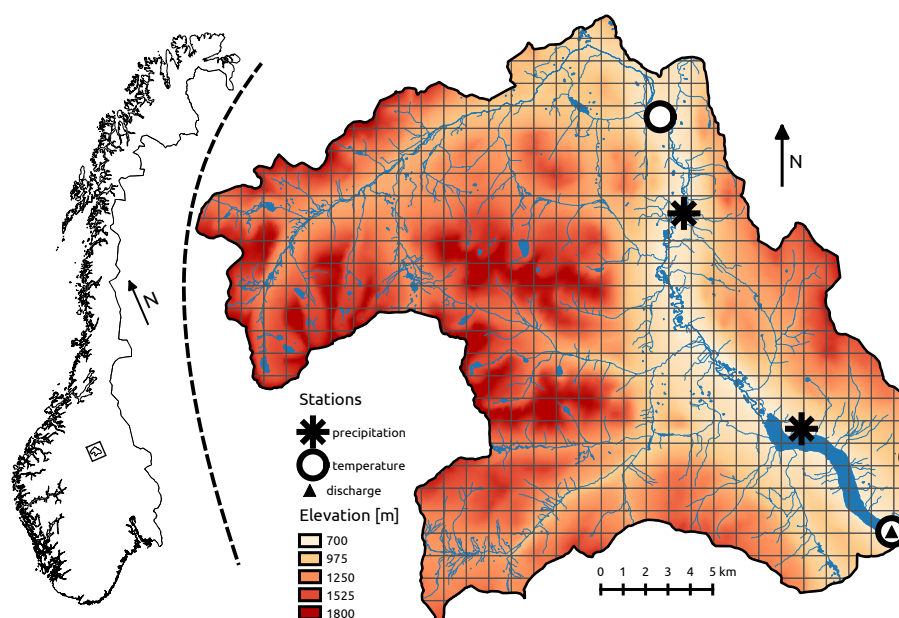

Figure 2. Location of the Atnsjoen catchment in Norway (black box in left map) and overview map of the Atnsjoen catchment (right).

Hydrology and
Earth System
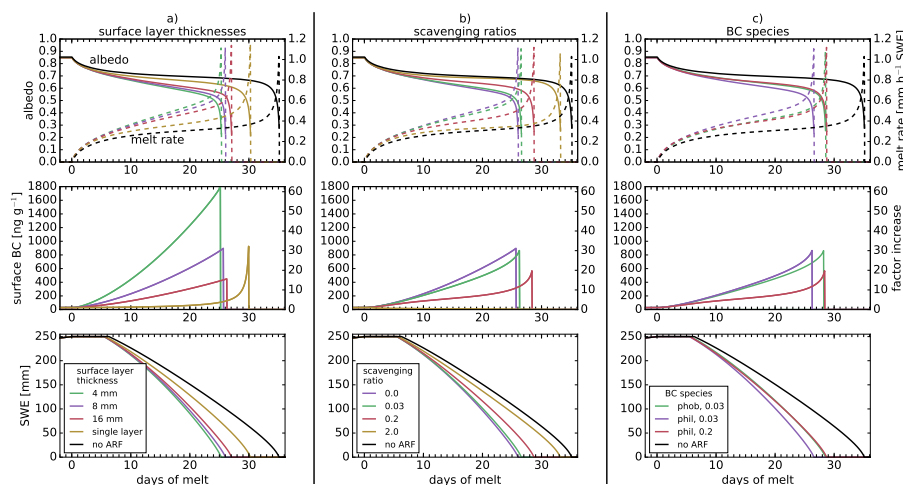Sciences
Discussions

Open Access

Figure 3. Snow albedo (top row of graphs; solid lines) and melt rate (top row of graphs; dashed lines), BC concentration in the surface layer and factor increase of the surface concentration during melt compared to the pre-melt surface concentration (central row of graphs), and snowpack SWE (bottom row of graphs) for simulations forced with synthetic data according to Table 3 and different model configurations: (a) different values for maximum surface layer thickness; (b) scavenging ratio; and (c) BC species with different melt scavenging ratios applied (*phob* and *phil* in legend stands for hydrophobic and hydrophilic BC, respectively). The black lines in all graph show simulation results of model runs without ARF applied (no ARF).
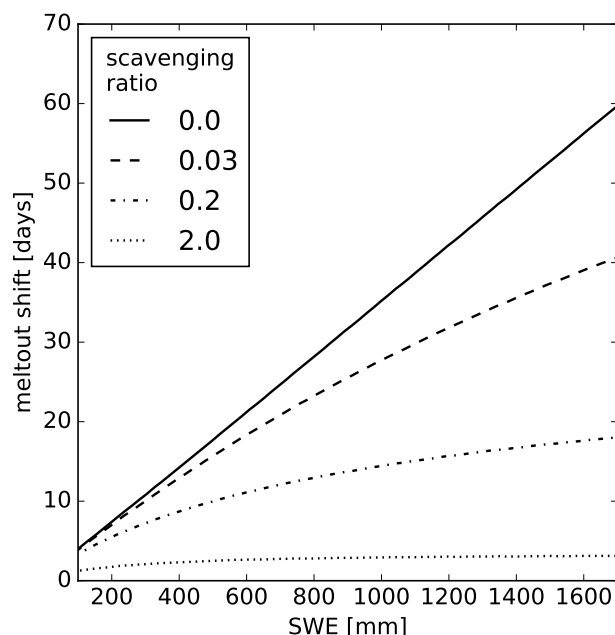

Figure 4. Shift in the day of meltout (y-axis) from simulations with different scavenging ratios compared to the respective scenario with ARF turned off using snowpacks of different magnitudes at melt-onset (x-axis) and same total BC mass.
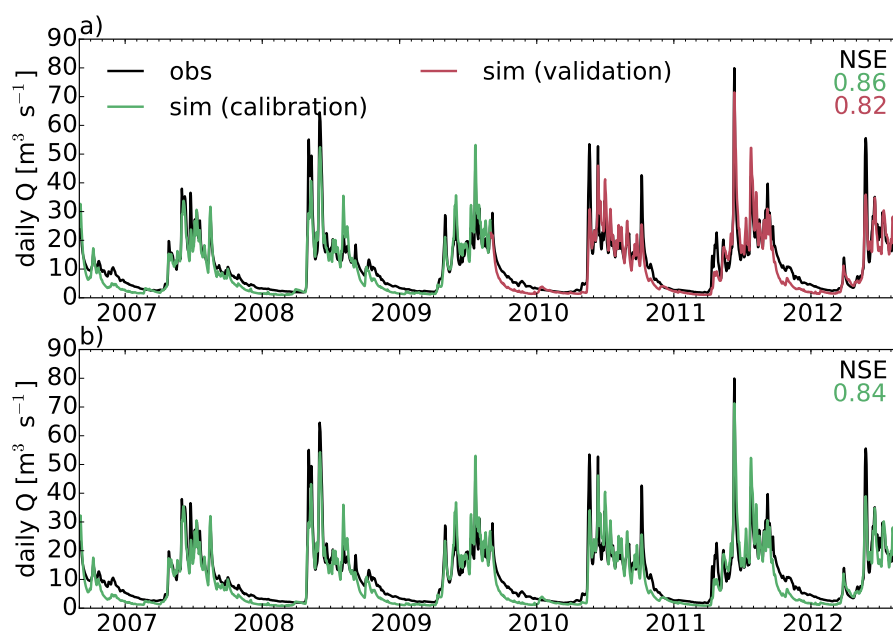
Figure 5. Simulated (green and red curves) and observed (black curve) daily discharge from the Atnsjoen watershed. Graph (a) is showing the simulation results for 3 years of calibration (green) and 3 years of validation (red). Graph (b) is showing the results for a 6 years calibration period.

Table 1. Information about observational stations.

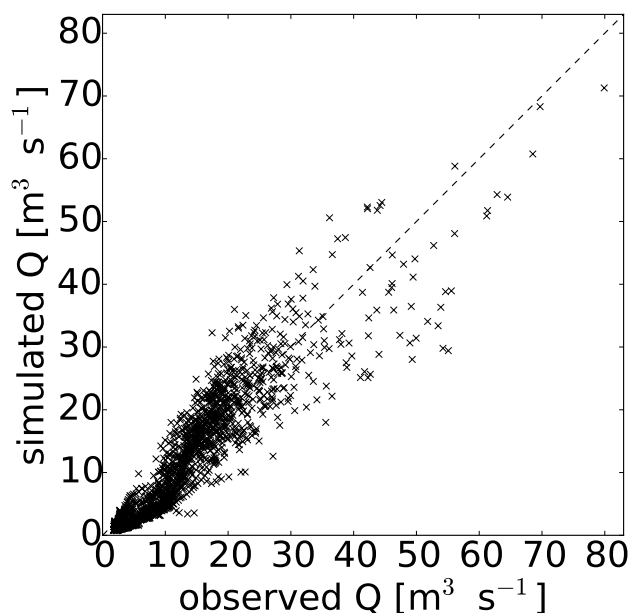| Station name	Station ID	Operator	Observational variable	Elevation
Atnsjoen 1	8720	MET	precipitation	749
Atndalen-Eriksrud	8770	MET	precipitation	731
Atnsjoen 2	2.32.0	NVE	temperature	701
Li Bru	2.479.0	NVE	temperature	780
Fokstuga	16610	MET	wind speed; relative humidity	973
Kvifjell	13160	MET	wind speed	1030
Venabu	13420	MET	relative humidity	930

123

Figure 6. Comparison of observed and simulated daily discharge Q of the Atnsjoen catchment. The dashed black line demonstrates perfect agreement between simulation and observation.

Table 2. Model settings for the scenario without Aerosol Radiative Forcing (no ARF), and the minimum (min), central (mid), and maximum (max) BC forcing estimates.

Estimate	surface layer [mm]	deposition factor	scavenging ratio phob	scavenging ratio phil
no ARF	-	0.0	-	-
mid	8.0	1.0	0.03	0.2
min	16.0	0.5	0.3	2.0
max	4.0	1.5	0.003	0.02

Table 3. Synthetic forcing data applied in the 1-D sensitivity study of Sect. 5.1. The applied forcing during the melt period are based on average observations during spring melt of the Atnsjoen catchment. BC deposition rate and precipitation during the snow accumulation period equals the respective catchment averages during snow accumulation in the Atnsjoen catchment.

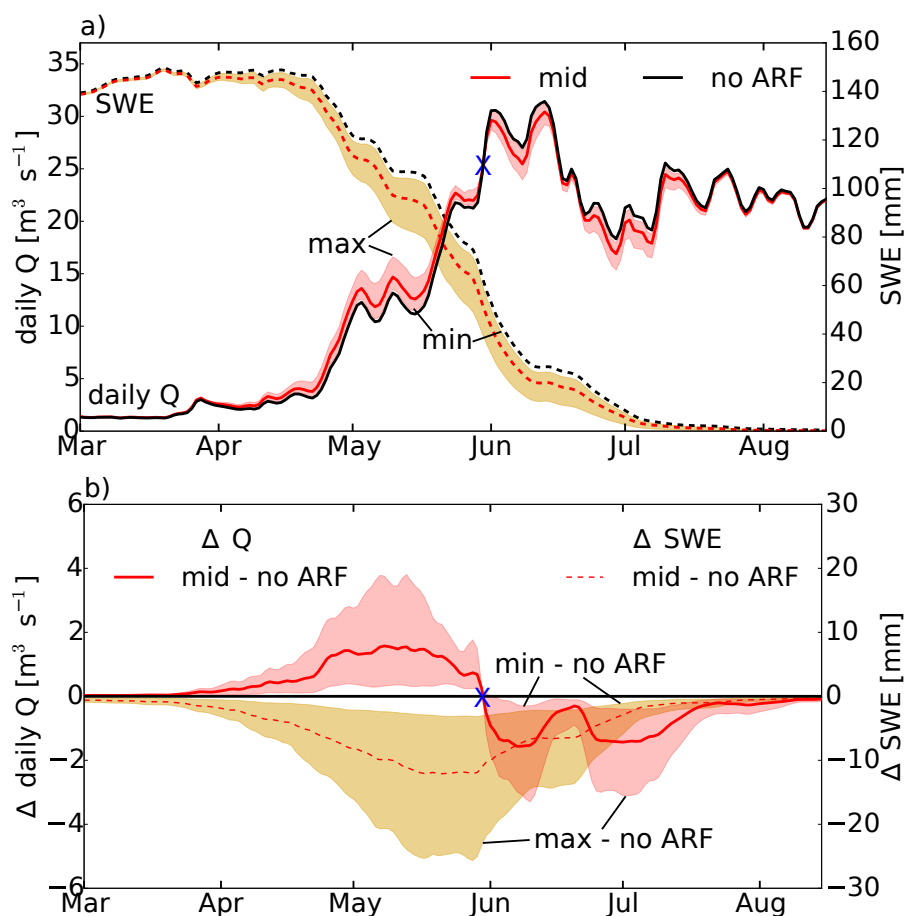| variable		accumulation period	melt period	unit
temperature		-5.0	5.0	C
precipitation		0.15	0.0	mm h-1
radiation		0.0	250.0	W m-2
BC deposition	no ARF	0.0	0.0	kg m-2 h-1
	ARF	1.65e-9		

Figure 7. (a) Simulated daily discharge (Q; solid lines) and catchment mean snow water equivalent (SWE; dashed lines) for the mid (red lines), low and high (shaded) estimates and for the scenario without ARF (no ARF; black lines) averaged over the 6 years period. (b) Differences in daily discharge and SWE of ARF scenarios to the scenario without ARF (no ARF). The blue marker in (a) and (b) separates the periods where BC in snow has an enhancing (left of marker) and a decreasing (right of marker) effect on the discharge.
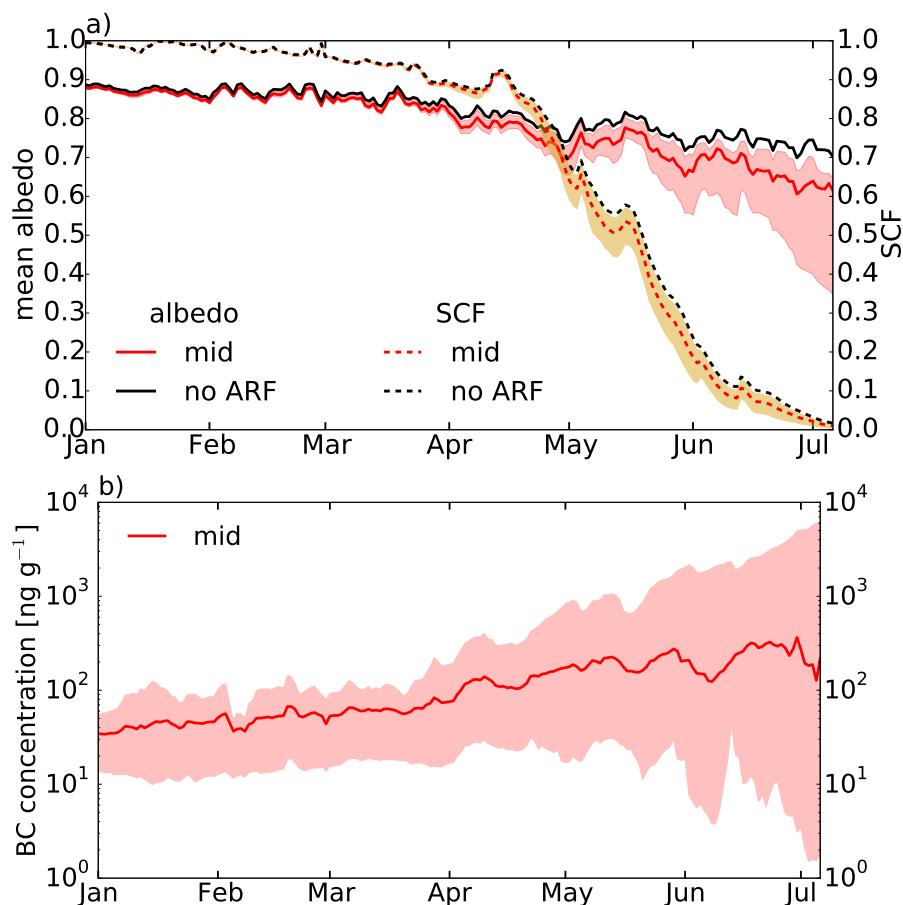
Figure 8. (a) Simulated mean catchment snow albedo (solid lines) and snow covered fraction (SCF; dashed lines) for the mid (red lines), low and high (shaded) estimates and for the scenario without ARF (no ARF; black lines) averaged over the 6 years period. (b) Concentration of BC in the surface layer of the model for the mid (solid line), min (lower bound of shaded area) and max (upper bound of shaded area) estimates.
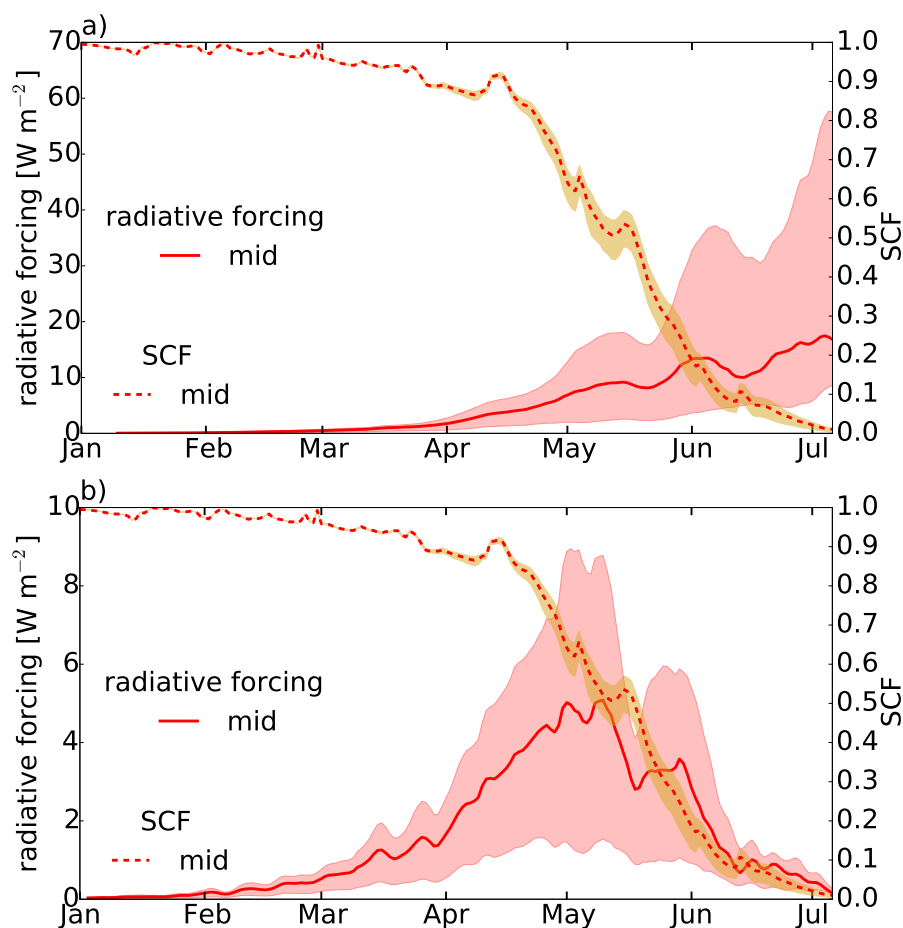
Figure 9. Catchment snow covered fraction (SCF; dashed lines) and (a) simulated mean radiative forcing in snow and (b) simulated mean radiative forcing normalized with the SCF for the mid (solid red lines), min (lower bound of shaded area) and max (upper bound of shaded area) estimates averaged over the 6 years period.